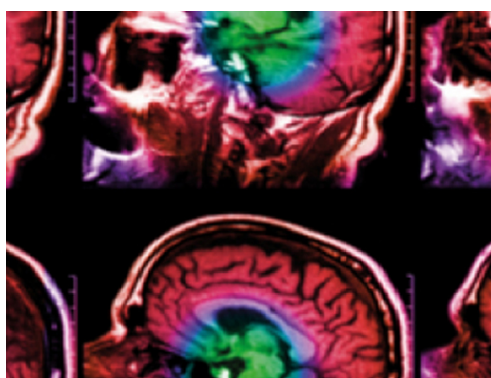


PAPER

## In silico feasibility assessment of extracorporeal delivery of low-intensity pulsed ultrasound to intervertebral discs within the lumbar spine

To cite this article: Matthew S Adams *et al* 2020 *Phys. Med. Biol.* **65** 215011

View the [article online](#) for updates and enhancements.



**IPEM | IOP**

Series in Physics and Engineering in Medicine and Biology


Your publishing choice in medical physics,  
biomedical engineering and related subjects.

Start exploring the collection—download the  
first chapter of every title for free.



## PAPER

# In silico feasibility assessment of extracorporeal delivery of low-intensity pulsed ultrasound to intervertebral discs within the lumbar spine

Matthew S Adams<sup>1</sup> , Jeffrey C Lotz<sup>2</sup> and Chris J Diederich<sup>1</sup> <sup>1</sup> Thermal Therapy Research Group, Department of Radiation Oncology, University of California San Francisco, 2340 Sutter Street, S341, San Francisco, CA 94115, United States of America<sup>2</sup> Department of Orthopaedic Surgery, University of California San Francisco, CA 94143, United States of AmericaE-mail: [Chris.Diederich@ucsf.edu](mailto:Chris.Diederich@ucsf.edu)**Keywords:** Low-intensity pulsed ultrasound, intervertebral discs, time reversal, back pain, spine, phased array, pulsed focused ultrasoundRECEIVED  
31 December 2019REVISED  
27 May 2020ACCEPTED FOR PUBLICATION  
3 July 2020PUBLISHED  
2 November 2020

## Abstract

Low intensity pulsed ultrasound (LIPUS) may have utility for non-invasive treatment of discogenic lower back pain through stimulating, remodeling and accelerating healing of injured or degenerated intervertebral disc (IVD) tissues. This study investigates the feasibility of delivering LIPUS to lumbar IVDs between L2 and S1 spine vertebra using a planar extracorporeal phased array (8 × 8 cm, 1024 elements, 500 kHz). Three 3D anatomical models with heterogenous tissues were generated from patient CT image sets and used in the simulation-based analysis. Time-reversal acoustic modeling techniques were applied to optimize posterior-lateral placement of the array with respect to the body to facilitate energy deposition in discrete target regions spanning the annulus fibrosus and central nucleus of each IVD. Forward acoustic and biothermal simulations were performed with time-reversal optimized array placements and driving amplitude/phase settings to predict LIPUS intensity distributions at target sites and to investigate off-target energy deposition and heating potential. Simulation results demonstrate focal intensity gain of 5–168 across all IVD targets and anatomical models, with greater average intensity gain (>50) and energy localization in posterior, posterolateral, and lateral target sites of IVDs. Localized LIPUS delivery was enhanced in thinner patient anatomies and in the high lumbar levels (L2-L3 and L3-L4). Multiple amplitude/phasing illumination patterns could be sequenced at a fixed array position for larger regional energy coverage in the IVD. Biothermal simulations demonstrated that LIPUS-appropriate exposures of 100 mW cm<sup>-2</sup> I<sub>SPTA</sub> to the target disc region would result in <1 °C global peak temperature elevation for all cases. Hence, simulations suggest that spatially-precise extracorporeal delivery of therapeutically relevant LIPUS doses to discrete regions of lumbar IVDs is feasible and may be useful in clinical management of discogenic back pain.

## 1. Introduction

Low back pain (LBP) is increasingly prevalent, with up to 84% of all adults in the general population expected to experience LBP at some point of their lives (Goubert *et al* 2004, Shaheed *et al* 2014). The societal cost of LBP is immense, with total costs exceeding \$100 billion per year in the United States, primarily attributable to lost wages and reduced productivity (Katz 2006). Studies have shown that the lumbar intervertebral discs (IVDs) are the most common etiology of chronic LBP in adults (Peng 2013), with discogenic LBP related to IVD degeneration accounting for about 40% of chronic LBP cases, and lower disc herniation accounting for 30% (Zhang *et al* 2009, Lotz *et al* 2012). Clinical interventions for discogenic LBP and herniation are primarily intended for palliative relief, often at the expense of the functional integrity and nominal biomechanics and composition of the IVDs and spinal column. Spinal fusions and artificial disc replacements are common surgical interventions for degenerative disc disease (Martin *et al* 2009, Malik *et al*

2013), but have limitations in terms of long-term efficacy, complications, and reoperation rates (Eliasberg *et al* 2016, Fujii *et al* 2019). Minimally invasive thermal interventions are utilized to destroy pain-causing infiltrating nerves within degenerated discs, but disrupt the nominal disc structure and composition, with many modalities exhibiting limited to moderate overall treatment efficacy (Helm *et al* 2017). Disc herniation is often treated through lumbar discectomy for immediate pain relief, but suffers from high recurrent herniation rates (Arts *et al* 2019). Conservative management options of degenerative disc disease and disc herniation, such as physical therapy, pharmacologic therapy, or epidural steroid or methylene blue injections can yield limited pain relief and high progression rates leading to more invasive treatment options (Fujii *et al* 2019, Arts *et al* 2019). Given some of the drawbacks of current treatments, there is a need for non-invasive treatment options for disc degeneration and herniation that do not compromise the functional integrity of the IVD and surrounding anatomy.

Low intensity pulsed ultrasound (LIPUS) has been investigated and applied for a wide range of orthopedic applications, including bone fracture healing (Pounder and Harrison 2008, Harrison *et al* 2016), and accelerating the healing of tendon, ligament (Takakura *et al* 2002, Sparrow *et al* 2005), and muscle injuries (Shu *et al* 2012). FDA approved clinical devices, such as the Exogen Bone Healing System, are typically placed on the skin surface in close contact to the target tissue. LIPUS exposure regimens typically consist of low applied temporal-average acoustic intensities (30–1000 mW cm<sup>-2</sup>) and frequencies (<1.5 MHz), and pulsed sonication settings (20% duty cycle, 1 kHz pulse repetition rate) intended to mechanically stimulate target cells and tissues while minimizing heating generation (Jiang *et al* 2019). Many studies in *in vitro* cell and animal models have provided preliminary support for the potential utility of LIPUS in the treatment or prevention of IVD degeneration. IVD degeneration is associated with abnormal expression and biosynthesis of inflammatory cytokines, and the breakdown of nominal extracellular matrix structure and composition (Risbud and Shapiro 2014). LIPUS has been demonstrated to induce an anti-inflammatory response and stimulate cell proliferation, proteoglycan production and matrix synthesis in IVD nucleus pulposus and annulus fibrosus cells (Iwashina *et al* 2006, Hiyama *et al* 2007, Omi *et al* 2008, Kobayashi *et al* 2009, Chen *et al* 2015), which may enhance water retention in IVDs, stimulate new collagen generation and potential strengthening in the annular wall, and reduce desiccation and herniation. Further, *in vitro* studies have demonstrated that LIPUS may accelerate herniated disc resorption (Iwabuchi *et al* 2005, 2008).

Extracorporeal high intensity focused ultrasound and phased array ultrasound platforms enable precisely controlled non-invasive delivery of ultrasound to specific tissue targets in the body. However, in consideration of target-specific localization of acoustic energy into IVDs from an extracorporeal source, ultrasound delivery may be complicated by the complex spine anatomy and irregular bone geometry, as bone is highly attenuating and causes significant reflections and distortion of the incident acoustic beam. Further, acoustic propagation across fat and other soft tissue layers causes beam refraction, degrading focusing capabilities and energy deposition accuracy, while gas-containing tissues such as bowel completely impede acoustic transmission. Time-reversal techniques have been demonstrated as an effective means of compensating for ultrasound beam distortion in heterogeneous tissue environments, including in transcostal and transcranial settings (Aubry *et al* 2008, Fink 1992, Thomas and Fink 1996, Fink *et al* 2004). Numerical modeling approaches have incorporated time-reversal in order to calculate necessary driving parameters (amplitude and phase settings) that can be applied to phased arrays in order to mitigate beam distortion, and have been experimentally validated to restore high quality focusing capabilities in complex anatomical environments (Aubry *et al* 2003, Marquet *et al* 2009). Qiao *et al* applied time-reversal modeling techniques to investigate the feasibility of generating high acoustic pressures and intensities within the nucleus of lumbar IVDs in order to generate localized inertial cavitation and fractionate the nucleus to facilitate partial disc replacement interventions (Qiao *et al* 2019). This study investigated a custom bilateral phased array with curvilinear geometry surrounding posterolateral aspects of the body, designed to produce a tight acoustic focus at the very center of the IVD. Alternative spine-specific bilateral phased array designs were investigated by Xu *et al* through multi-layered ray acoustics modeling for generating acoustic foci within the thoracic spinal canal via paravertebral, translaminar, and transvertebral pathways for blood-spinal cord barrier opening applications (Xu and O'Reilly 2020).

The objective of this current study was to apply time-reversal modeling methods and simulations to explore the feasibility of delivering localized, therapeutically-relevant LIPUS doses to various regions of lumbar IVDs using an extracorporeal phased array source. Here a generic planar (8 cm square profile, 32 × 32 elements, 0.5 MHz) phased array design that is similar to commercially available platforms was utilized. An operating frequency of 0.5 MHz was selected as a balance of deep target access, minimization of temperature elevation in bone and surrounding structures, and spatial localization capability, as similarly applied in other studies and array designs investigating ultrasound delivery to IVDs and spinal targets (Qiao *et al* 2019, Xu and O'Reilly 2020). Simulations incorporated 3D human anatomical models with

**Table 1.** Summary of relevant anatomical characteristics across the models incorporated in study.

Model	Age/gender	Waist perimeter (cm)	L2-L3 disc height (mm)	L3-L4 disc height (mm)	L4-L5 disc height (mm)	L5-S1 disc height (mm)	Avg. disc height (mm)	Iliac crest to mid L4-L5 height dist. (mm)
I	51/M	69	6.2	5.9	5.7	7.5	6.3	1
II	52/F	95	6.7	6.3	6.2	3.6	5.7	13
III	82/M	96	6.7	7.1	6.6	5.8	6.5	-14

heterogeneous tissues and targets located throughout the annulus fibrosus and nucleus in IVDs spanning the L2-S1 vertebral levels. Backward virtual source simulations were performed to identify optimal array placements posterior/posterolateral to the body and time-reversed phase and amplitude driving settings tailored to facilitate energy delivery to each target IVD region. Corresponding forward acoustic and biothermal simulations using the extracorporeal phased array were performed, and metrics were derived from the resultant acoustic intensity and temperature distributions to assess the energy localization for each target region and the presence of significant off-target energy deposition and undesired heating potential. The capability of increasing spatial coverage of acoustic energy to larger IVD regions was also explored by interleaving multiple phasing/amplitude array illumination patterns for a fixed array position.

## 2. Methods

### 2.1. Generation of 3D anatomical models

3D anatomical tissue models were generated for the simulations using anonymized human CT image sets, spanning from the pelvis to the T12 vertebra, with slice thickness of 1–1.5 mm and in-plane pixel resolution of 0.7–0.78 mm. Three CT image sets were incorporated and converted to 3D models to selectively investigate the influence of different body sizes and anatomical variation on LIPUS delivery to IVDs. The three generated models will be referred to as Model I, Model II, and Model III, with relevant details and dimensions of each described in table 1.

The CT image sets were imported into Mimics Innovation Suite (Materialise, Belgium) for segmentation of relevant anatomical structures and tissues, including skin, fat, muscle, cortical bone, cancellous bone, spinal cord, lumbar nerve branches, bowel, kidney, major vasculature (aorta and inferior vena cava), and IVD. A combination of manual, semiautomatic, and automatic segmentation techniques, including contouring, dynamic region growing, thresholding, and morphological operations were used to perform the segmentations. IVD tissue was segmented and modeled as a single tissue compartment, due to lack of contrast between the nucleus and annular walls regions within the CT images. Cortical bone was approximated as the outer 1.5 mm thick layer for all bone structures to simplify the segmentation process, with all internal bone structure modeled as cancellous bone. In Model III the inferior vena cava was omitted due to poor CT contrast. Representative CT images, segmented axial tissue slices through each of the IVDs between L2 and S1, and the full 3D model for each anatomical model are shown in figure 1. Acoustic and biothermal tissue properties adopted for all modeled tissues are listed in table 2 (Hynynen 1990, Nicholson *et al* 1994, Duck 2013, Scott *et al* 2014, Hasgall *et al* 2018).

For each anatomical model, seven generalized target points in each of the L2-L3, L3-L4, L4-L5, and L5-S1 IVDs were investigated via simulations to assess the feasibility of targeted extracorporeal LIPUS delivery. These target points were placed in the posterior, posterolateral, lateral, anterolateral, anterior, medial, and mediolateral regions of each IVD, as shown in figure 2, to generalize LIPUS accessibility to each region. Unilateral targets were investigated for each IVD, due to presumed lateral symmetry. For Models I and III, the target points spanned the left lateral side of the IVDs, whereas for Model II target points spanned the right side.

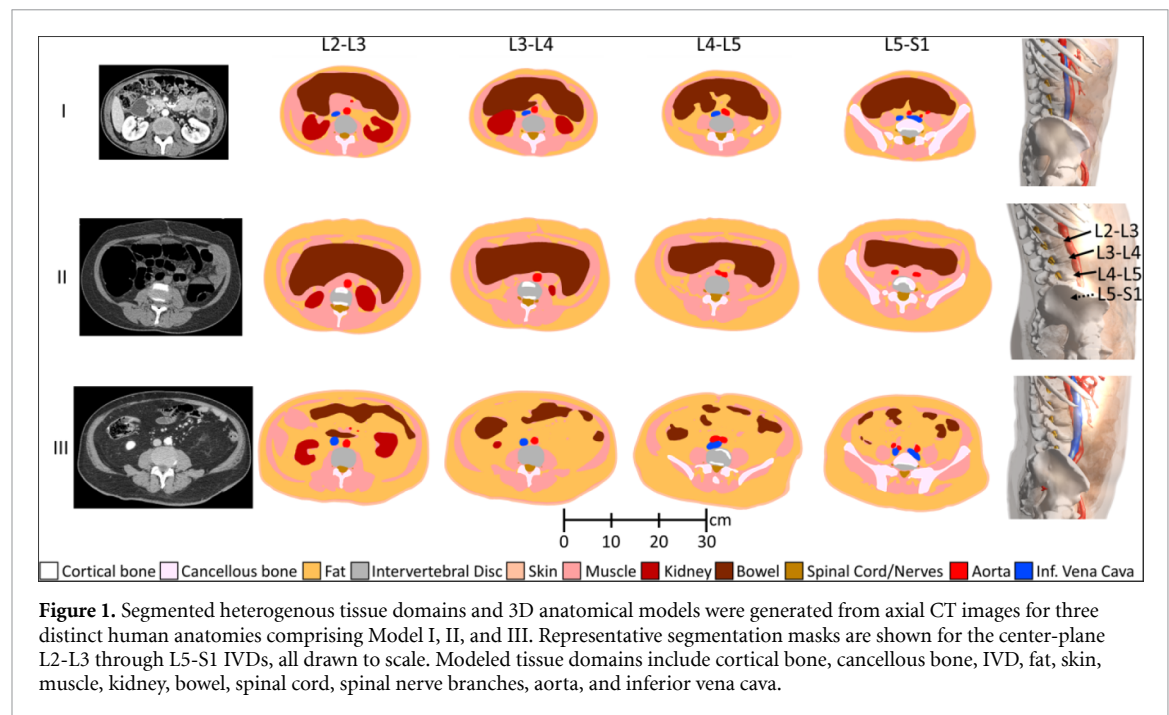
### 2.2. Acoustic and biothermal simulations

A planar extracorporeal ultrasound phased array was modeled herein for acoustic simulations of LIPUS delivery. The overall dimensions of the square array were 80 × 80 mm, consisting of 1024 square elements arranged in a uniform 32 × 32 cartesian grid, with 2.5 mm pitch and 0.2 mm kerf width, operating at 500 kHz. The surface of the array was offset from the body surface, with the properties of water modeled between.

The acoustic and biothermal simulations were performed using Sim4Life 4.4 (Zurich Med Tech AG, Switzerland). Acoustic modeling was performed using a finite difference time-domain solver of the 3D linear acoustic pressure wave equation (LAPWE), which incorporates relevant wave propagation phenomena including diffraction, interference, reflection, refraction, and attenuation. Modeling of non-linear wave propagation was not incorporated, as the target intensities typical of LIPUS exposure are well below

**Table 2.** Acoustic and thermal tissue properties used in simulations.

Tissue	Density (kgm <sup>-3</sup> )	Speed of sound (m/s)	Attenuation (Np/m) at 0.5 MHz	Thermal conductivity (W/m/°C)	Specific heat capacity (J/kg/°C)	Perfusion (ml/min/kg)
Cortical bone	1908 <sup>d</sup>	3514.9 <sup>d</sup>	75 <sup>b,c</sup>	0.32 <sup>d</sup>	1313 <sup>d</sup>	10 <sup>d</sup>
Cancellous bone	1178 <sup>d</sup>	2117.5 <sup>d</sup>	72.5 <sup>e</sup>	0.31 <sup>d</sup>	2274 <sup>d</sup>	30 <sup>d</sup>
Fat	911 <sup>d</sup>	1440 <sup>d</sup>	3.5 <sup>c</sup>	0.21 <sup>d</sup>	2348 <sup>d</sup>	33 <sup>d</sup>
Intervertebral disc <sup>a</sup>	1142 <sup>d</sup>	1750 <sup>d</sup>	6.44 <sup>d</sup>	0.47 <sup>d</sup>	3432 <sup>d</sup>	0 <sup>f</sup>
Skin	1109 <sup>d</sup>	1624.0 <sup>d</sup>	10.58 <sup>d</sup>	0.37 <sup>d</sup>	3391 <sup>d</sup>	106 <sup>d</sup>
Muscle	1090 <sup>d</sup>	1588.4 <sup>d</sup>	3.36 <sup>d</sup>	0.49 <sup>d</sup>	3421 <sup>d</sup>	37 <sup>d</sup>
Kidney	1066 <sup>d</sup>	1554.3 <sup>d</sup>	3.7 <sup>d</sup>	0.53 <sup>d</sup>	3763 <sup>d</sup>	3795 <sup>d</sup>
Bowel	1045 <sup>d</sup>	1540 <sup>c</sup>	3 <sup>b</sup>	0.56 <sup>d</sup>	3801 <sup>d</sup>	0 <sup>d</sup>
Spinal cord	1075 <sup>d</sup>	1542 <sup>d</sup>	6.18 <sup>d</sup>	0.51 <sup>d</sup>	3630 <sup>d</sup>	160 <sup>d</sup>
Nerve	1075 <sup>d</sup>	1629.5 <sup>d</sup>	6.18 <sup>d</sup>	0.49 <sup>d</sup>	3613 <sup>d</sup>	160 <sup>d</sup>
Blood	1050 <sup>d</sup>	1578 <sup>d</sup>	1.14 <sup>d</sup>	—	—	—
Water	1000 <sup>d</sup>	1500 <sup>d</sup>	0	0.6 <sup>d</sup>	4178 <sup>d</sup>	0

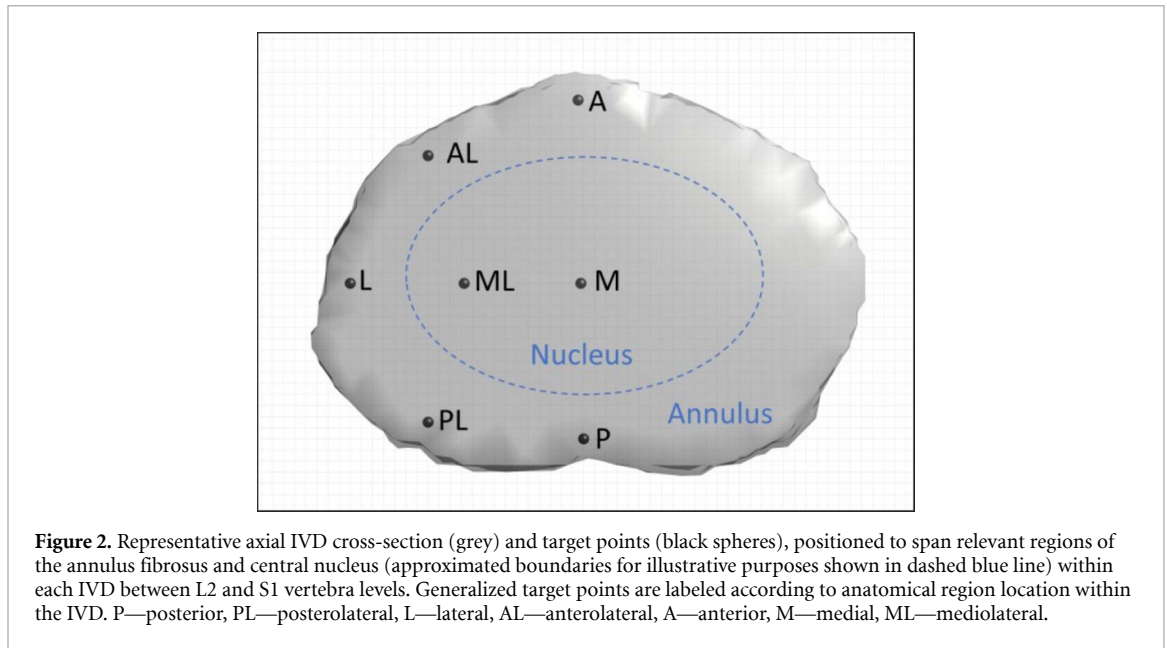
<sup>a</sup>Properties of tendon/ligament used.<sup>b</sup>(Duck 2013)<sup>c</sup>(Hynynen 1990)<sup>d</sup>(Hasgall *et al* 2018)<sup>e</sup>(Nicholson *et al* 1994)<sup>f</sup>(Scott *et al* 2014)

non-linear intensity thresholds (Muir and Carstensen 1980). The formulation of the LAPWE used in Sim4Life is as follows:

$$\rho \nabla \cdot \frac{1}{\rho} \nabla p - \frac{1}{c^2} \frac{\delta^2 p}{\delta t} - \frac{2\alpha}{c^2} \sqrt{\frac{\alpha^2 c^4}{\Omega^2} + c^2} \frac{\delta p}{\delta t} = 0, \quad (1)$$

where  $\rho$  is density,  $p$  is pressure,  $c$  is speed of sound,  $t$  is time,  $\alpha$  is absorption coefficient (Np/m), and  $\Omega$  is angular frequency. STL files of all the 3D tissues and anatomical structures for each Model were imported into the Sim4Life modeling environment, and built-in parameterized computer-aided design tools were used to generate the phased array structure and transducer elements. The acoustic surface velocity and phase were modeled as uniform over the radiating surface of each phased array element. Thermal simulations were performed using a direct matrix solver of the steady-state form of Pennes Bioheat Equation, as formulated below:





$$\nabla \cdot (k\nabla T) + Q - \rho_b c_b \omega (T - T_b) = 0 \quad (2)$$

where  $k$  is thermal conductivity,  $T$  is temperature,  $\rho_b$  is the density of blood,  $c_b$  is the specific heat of blood,  $T_b$  is blood temperature ( $37^\circ\text{C}$ ),  $\omega$  is perfusion rate, and  $Q$  is the acoustic power deposition, as below:

$$Q = 2\alpha I = \alpha \frac{p^2}{\rho c} \quad (3)$$

where  $I$  is the spatial peak, temporal average acoustic intensity. For acoustic and thermal simulations the maximum element size was set to 0.28 mm and 0.5 mm, respectively, based on mesh convergence studies demonstrating solution accuracy. The temporal discretization for the acoustic simulations was 35 ns, and the time duration simulated was equivalent to the number of acoustic periods needed for the wave to reach the end of the computational domain, plus a safety factor of 60 periods ( $\sim 200$  mm additional propagation distance) to account for reflections. The acoustic source was active during the entire simulation duration, corresponding to an average of 140 periods or cycles. Perfectly matched layers were used on all domain boundaries to prevent reflections at the boundaries of the computational domain.

### 2.3. Backwards projection from target point

For each Model and IVD target point, a spherical virtual acoustic point source generating a 500 kHz sinusoidal pressure waveform was positioned at the respective target point, and a backwards acoustic simulation was performed to propagate the emitted pressure waveform outside the body surface to regions where the extracorporeal array may be positioned (figure 3(a)). The computational grids for these backwards simulations extended  $\sim 50$  mm beyond the lateral and posterior body surface boundaries and extended  $\sim 150$ – $200$  mm along the longitudinal body axis. The tissue acoustic properties listed in table 2 were applied. The calculated complex pressure distribution for each of these simulations was saved and imported into MATLAB for post-processing, as described below.

### 2.4. Determination of optimal array positioning

A grid search process was used to determine the optimal array position for the forward acoustic simulation for each target point (figure 3). The array position was initialized at the posterior edge of the model, as shown in figure 3(b), with the virtual point source aligned with the central axis of the array. The array was successively rotated about the point source in  $2.5^\circ$  angular steps, with the total angular extents about the longitudinal ( $\theta$ ) and lateral ( $\phi$ ) axes up to  $120^\circ$  and  $70^\circ$ , respectively, depending on model and target point location. Only posterior/lateral alignments of the array with respect to the body were considered, as anterior application was considered impractical due to potential interference of acoustic propagation by gas-filled bowel. At each angular position, first interference checks were performed to ensure the array was outside the body, and if not, the array was translated backwards along the central axis in 5 mm steps between successive interference checks. Interference checks of the overlap of the array and anatomical model was determined in Matlab, by first discretizing the transformed array surface into points (with coordinates of each). STL files of

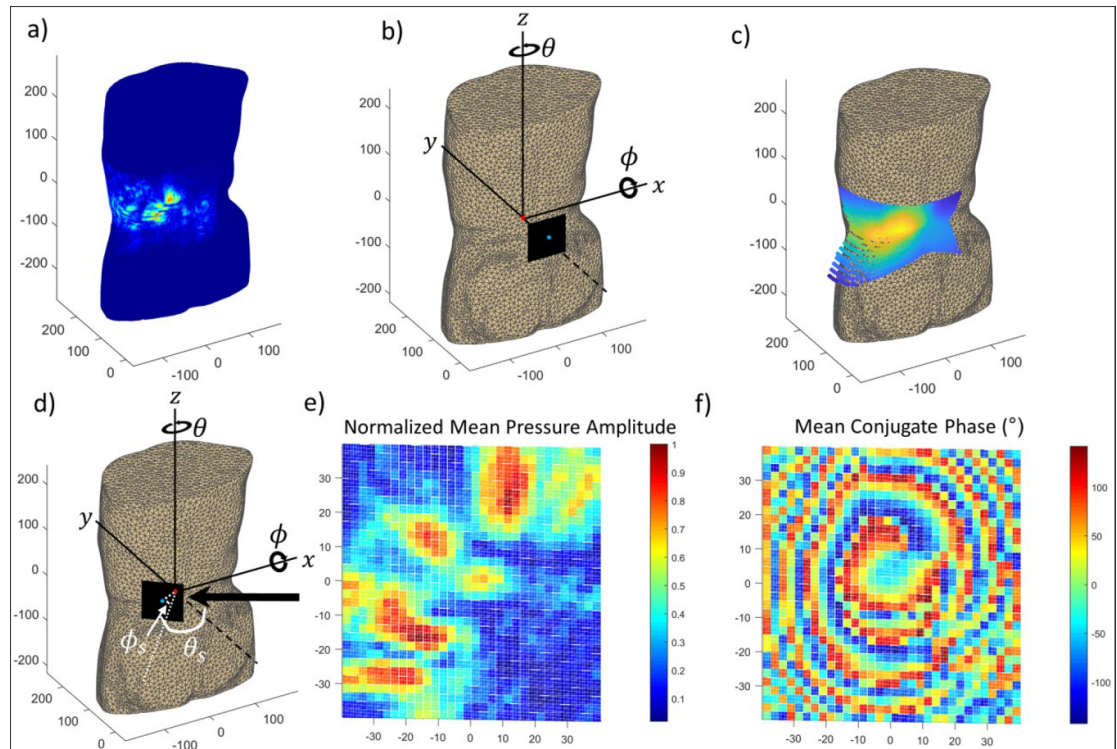


**Figure 3.** Workflow and grid search process for determination of optimized array position and array driving settings. First, for each target point, a virtual acoustic point source was placed at its position, and backwards acoustic simulations were performed to propagate the spherically radiating pressure emissions to outside the body. (a) The 3D pressure emissions magnitude distribution, as interpolated on the surface of the anatomical model for illustrative purposes, is indicative of where greatest amounts of emitted energy exit the anatomical model boundaries. (b) The array position was initialized at the proximal skin boundary, transversely centered on the target point, and rotated step-wise about the  $x$  and  $z$  axes by  $\theta$  and  $\phi$  degrees, respectively, through a pre-defined search grid. At each rotational position, the 3D pressure emission magnitude distribution was spatially interpolated and summed over the array surface, and the summed value was plotted to generate a spatial map of energy density across all array positions, as shown in (c). (d) The array position resulting in maximum pressure magnitude sum ( $\theta_s$ ,  $\phi_s$ ) was selected, and interpolated pressure amplitude, normalized to 1, and conjugate phase settings ( $^\circ$ ), averaged across each array element were applied as driving settings to the array elements, as shown in (e) and (f), respectively, for the corresponding forward acoustic/biothermal simulations. This workflow was used for all combinations of target point, IVD, and anatomical model. All axis units are in millimeters.

the anatomical model, as generated in Mimics Innovation Suite, were imported into Matlab, and the Inpolyhedron function was used to test that none of the discretized array surface coordinates were within the space occupied by the anatomical model. Once interference passed, for each angular position the pressure magnitude distribution, as generated from the backwards virtual source simulation described above, was spatially interpolated across the discretized array surface using the griddedInterpolant MATLAB function with linear interpolation method, and summed across all discretized array surface points to a total pressure sum value. Surface maps of these pressure sums were generated across the extracorporeal rotational search space, as shown in figure 3(c), and the array position resulting in the maximum pressure sum value was chosen for the corresponding forward simulation.

### 2.5. LIPUS distributions—single point targets

A forward acoustic simulation was performed for each target point using the planar phased array as the acoustic source, with the array placed in the respective optimized position. Element-specific amplitude and phase driving settings were determined by interpolating and taking the average of the normalized pressure amplitude and conjugate phase values from the corresponding backwards simulation pressure distribution across each element of the array. A water bolus (water domain) was modeled to couple acoustic energy emitted by the phased array to the skin surface. To model worst case conditions, bowel tissue was modeled as gas-filled and perfectly reflecting. The resultant acoustic intensity distribution was analyzed, then uniformly scaled such that the peak intensity  $I_{\text{SPTA}}$  within 1 mm of the target point position, as a conservative accuracy requirement, was  $100 \text{ mW cm}^{-2}$ , selected as a mid-range LIPUS exposure value (Jiang *et al* 2019). This scaled intensity distribution was incorporated into the acoustic power deposition term (equation (3)) of Pennes Bioheat Equation for the forward biothermal steady-state simulation, to quantify temperature increases associated with extracorporeal LIPUS in the spine, and investigate the presence of substantial

off-target heating. For forward acoustic and thermal simulations, the transverse extent of the computational domain was  $160 \times 160$  mm, as centered about the phased array, and longitudinally extended 100 mm beyond the target point (in total 155–290 mm axially distal to the array depending on anatomy, target, and optimized array placement). Acoustic and thermal tissue properties in table 2 were applied. For thermal simulations convective boundary conditions were applied to the aorta and inferior vena cava (Haemmerich *et al* 2003). Dirichlet conditions were applied to constrain computational domain boundaries to 37 °C. Generated acoustic intensity and temperature distributions were exported to MATLAB for analysis.

## 2.6. LIPUS distributions—multi-point targets

In order to investigate the capability of producing larger volumetric and spatial coverage in the posterior and lateral regions of the annular wall, sequentially applied phasing patterns from a fixed array position was implemented for select anatomical and IVD target region cases. For each simulation, five target points and acoustic virtual point sources, each 4–5 mm apart, were placed along the periphery of the IVD. Determination of the optimal array position was performed as described above, using the backward pressure emissions from the centermost virtual point source. Given this single optimal array position, separate normalized pressure amplitude and conjugate phase settings were then determined for each of the five-point source backwards simulation pressure distributions. These input settings were applied for the series of forward acoustic simulations, corresponding to sequential electronic focusing at each of the five target points for a fixed array position.

## 2.7. Computational specifications

All simulations were performed using a PC workstation with an AMD Threadripper 2950  $\times$  3.5 GHz 16-Core Processor, 64 GB DDR4-2666 RAM, and dual GeForce GTX 1080 Ti 11 GB GPUs. Acoustic simulation sizes ranged from 250–500 million elements and were computed using the accelerated GPU solver within Sim4Life, for 20–55 min run times. Steady-state thermal simulations consisted of 34–64 million elements and computation times were 15–35 min.

## 3. Results

The optimized positions of the phased array determined for each IVD and target point location is illustrated in figure 4 for Model I–III, with mean and individual values of the optimal rotation angles ( $\theta_s, \phi_s$ ) about the longitudinal and lateral body axes, respectively, for each case detailed in figure 5. For all posterior target points, the optimal array alignment was determined to be posterior to the body, sonicating via the transforaminal pathway between spinal processes through the spinal canal. Varying posterolateral alignment was determined optimal for all other target point regions in IVDs between L2 and L5 vertebrae. For the L5-S1 IVD, the array placement for all target points except for those in posterolateral and lateral regions in Model I and II were primarily posterior, with energy delivery through the spinal canal. The mean axial distance of the positioned array from the target point for each anatomical model was 9.5 cm for Model I (range: 5.5–13 cm), 12.1 cm for Model II (range: 7.5–17 cm), and 13.1 cm for Model III (range: 9–19 cm).

Forward acoustic simulations were applied using the optimal array positioning and corresponding amplitude/phasing patterns across all target points and models, with example resultant intensity gain distributions shown in figure 6 for the target points of the Model I L3-L4 IVD. Intensity gain was calculated as the peak intensity within 1 mm of the target point, divided by the mean intensity at the array surface. A compilation of intensity gain data for all target points is detailed in figure 7 for each case, with averages across the three models shown for each combination of IVD level and target point region. While intensity gain  $>1$  was achieved for all target points, secondary intensity hotspots that were spatially off-target were also produced in many cases. Data of the distance between the target point and the spatial position of the global intensity maximum of the entire computation domain is similarly presented in figure 8. These data illustrate that posterior, posterior-lateral, and lateral target point regions had more concentrated and target-specific localization of acoustic energy and intensity gain compared to more anterior and central regions. Further, energy localization was generally greatest in the L2-L3 IVD and lowered successively down the spinal column to L5-S1, with some exceptions in posterior/posterolateral target point regions. The average intensity gain across all target points was 60.3 (range: 10–141) for Model I, 49.6 (range: 6.5–144) for Model II, and 31.1 (range: 4.5–89) for Model III. The spatial discrepancy between the position of the maximum acoustic intensity and target point was less than 5 mm in 12/28 (43%) target points in Model I, 11/28 (39%) target points in Model II, and 6/28 (21%) target points in Model III. Across all models, the field position of the intensity maximum was within the disc for 41/84 (49%) target points, in spinal cord/branches for 5/84 (6%) target points, and in adjacent soft tissue for 38/84 (45%) target points.



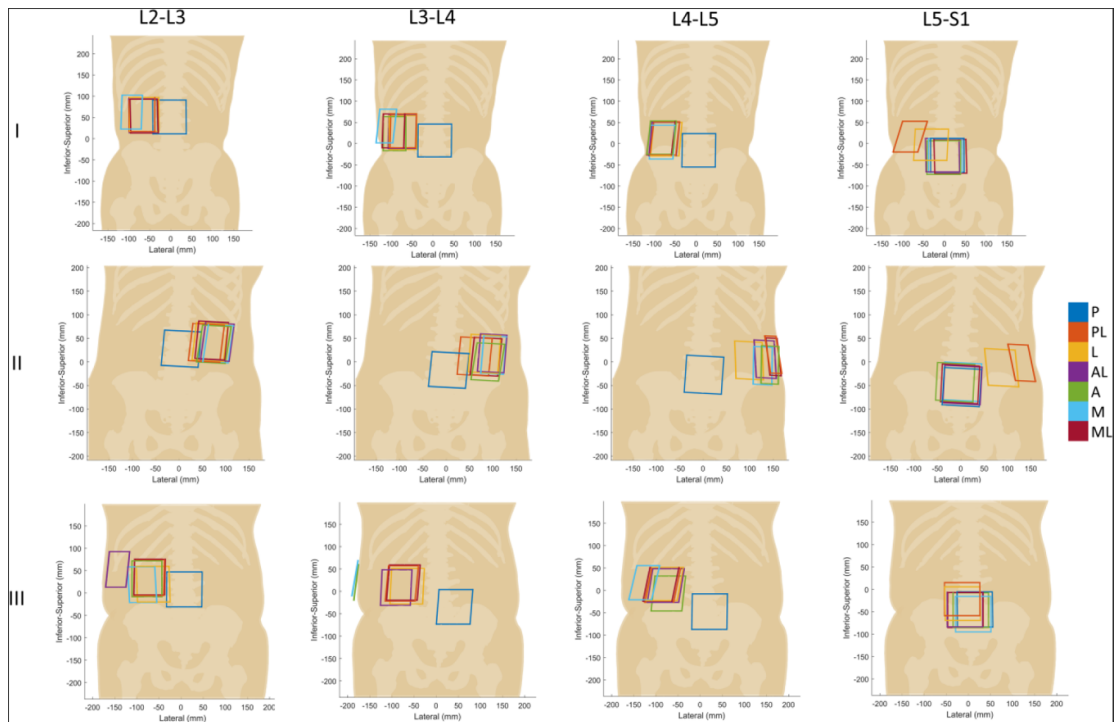


**Figure 4.** Posterior views for Model I-III depicting the optimized placement of the phased array determined to enhance energy delivery to IVD regions targeted in simulations. Optimal array positions and orientations, represented by the array outer border are shown for each model (rows), IVD level (columns), and target point region as color-coded in the legend. The corresponding optimal rotation angles about the longitudinal ( $\theta_s$ ) and (b) lateral ( $\phi_s$ ) body axes for each array position are shown in figure 5.

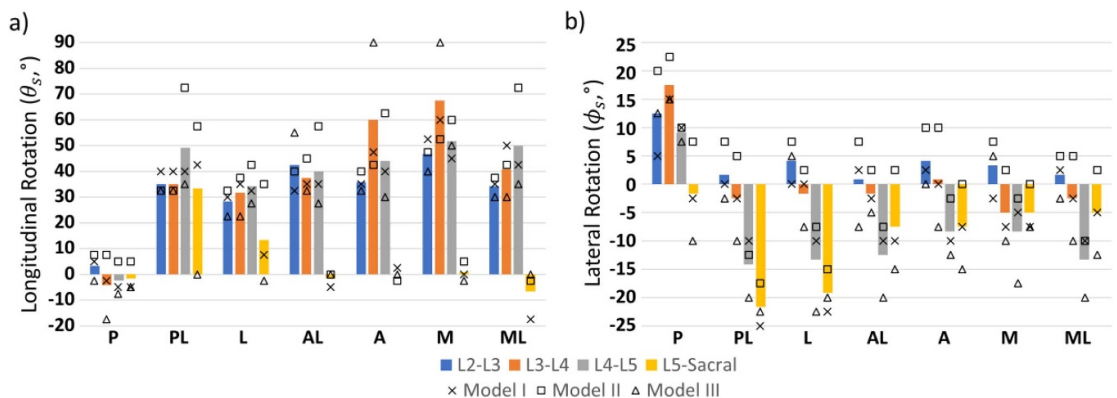


**Figure 5.** Optimal rotation angles of the phased array about the (a) longitudinal ( $\theta_s$ ) and (b) lateral ( $\phi_s$ ) body axes, as a function of target point region (horizontal axis), IVD level (vertical columns, color-coded), and anatomical model. The mean angle across the three models is given by the colored-bar, and the individual values for each model is provided by the symbols, for each IVD level and target point region combination. Rotation angle about the longitudinal axis is zero at posterior alignment of the array to the body and increases as it is laterally rotated about the body, ipsilateral to the target regions. Positive rotation angle about the lateral axis corresponds to progressive tilting up of the array face towards to the superior end of the model.

For biothermal simulations, example steady-state temperature elevation distributions corresponding to the intensity distributions shown in figure 6, scaled to a peak  $I_{SPTA}$  of  $100 \text{ mW cm}^{-2}$  within 1 mm of the target point, are shown in figure 9. Compilations of the global maximum temperature rise, and the maximum temperature rise in sensitive tissue structures, including the spinal cord and spinal nerve branches, are shown in figure 10. Global maximum temperature elevation was less than  $1^\circ\text{C}$  for all target points and models. Simulations in posterior/lateral target point regions resulted in lower temperature elevations compared to anterior and central targets. The mean maximum temperature elevation across all target points and models was  $0.20^\circ\text{C}$ ,  $0.25^\circ\text{C}$ ,  $0.30^\circ\text{C}$ , and  $0.37^\circ\text{C}$  for the L2-L3, L3-L4, L4-L5, and L5-S1 IVDs, respectively. The mean maximum global temperature rise across all target points was  $0.23^\circ\text{C}$  (range:  $0.08^\circ\text{C}$ – $0.6^\circ\text{C}$ ) for Model I,  $0.26^\circ\text{C}$  (range:  $0.09^\circ\text{C}$ – $0.72^\circ\text{C}$ ) for Model II, and  $0.35^\circ\text{C}$  (range:  $0.11^\circ\text{C}$ – $0.92^\circ\text{C}$ ) for Model III.

Lastly, multi-focus intensity distributions that can be sequentially applied with a single fixed array position are illustrated for posterolateral coverage of the L3-L4 IVD of Model I in figure 11, and for posterior

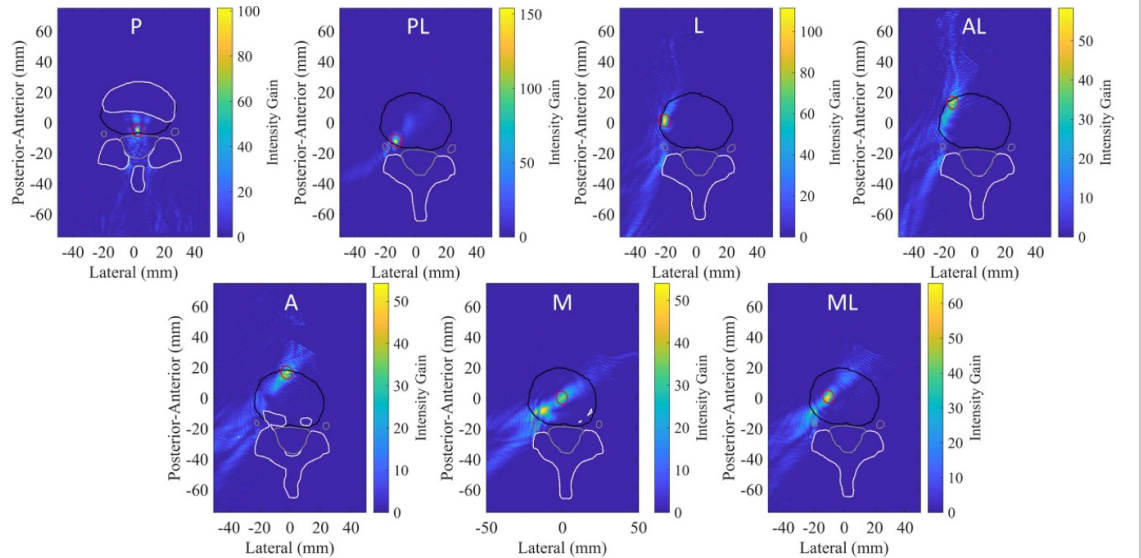


**Figure 6.** Axial intensity gain distributions in the L3-L4 IVD of Model I, for all seven target points as labeled by IVD region. Enhanced localization of acoustic energy and higher intensity gain was achieved in the posterior, posterolateral, and lateral target point regions of the IVD. Anatomical boundaries are contoured for bone (white), IVD (black) and spinal cord and nerve branches (grey). The target point is spatially located at the center of the red contour. For these example cases, peak intensities were localized within 1 mm of that target point for all locations except the Medial target case, in which a proximal hot-spot with 1.6 times the intensity amplitude of the target point was generated.

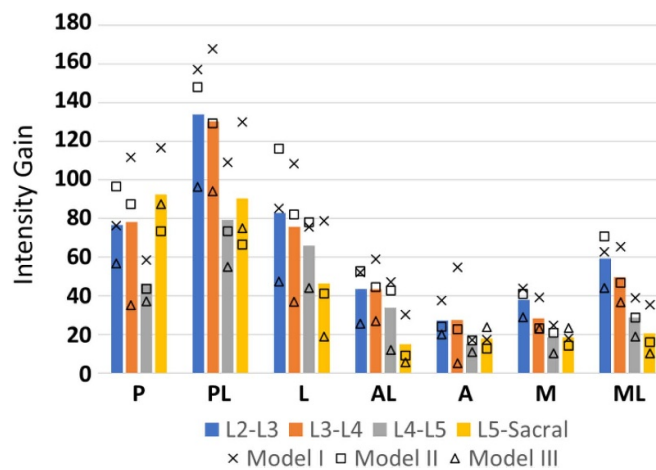


**Figure 7.** Compilation of acoustic intensity gain data as a function of target point region (horizontal axis), IVD level (vertical columns, color-coded), and anatomical model. The average gain value across models is given by the colored-bar, and the individual values for each model is provided by the symbols, for each IVD level and target point region combination. The intensity gain was defined as the maximum intensity within 1 mm of the target point, divided by the average array surface intensity.

coverage of the L5-S1 IVD of Model III in figure 12. The intensity gains across the five target point positions within the target region varied from 109–170 for the L3-L4 case, and 52–106 for the L5-S1 case.

#### 4. Discussion

This study utilized acoustic simulations and time-reversal methods to assess the feasibility of delivering localized LIPUS to target regions spanning the periphery and center of lumbar IVDs for three anatomical models derived from CT scans. Thermal simulations were incorporated to determine which IVD target regions have a higher relative risk of potentially damaging off-target energy deposition and heating. Simulation results illustrated that the capability of localized energy delivery was greatest in the posterior, posterolateral, and lateral peripheral regions of IVDs, with an overall average target intensity gain >50 across all Models and vertebral levels, as well as minimum temperature elevation and relative spatial discrepancy of peak intensity. Although anterior, medial, mediolateral and anterolateral targets had the lowest gain, poorest spatial specificity, and highest temperature elevation, acoustic intensity distributions within the disc were

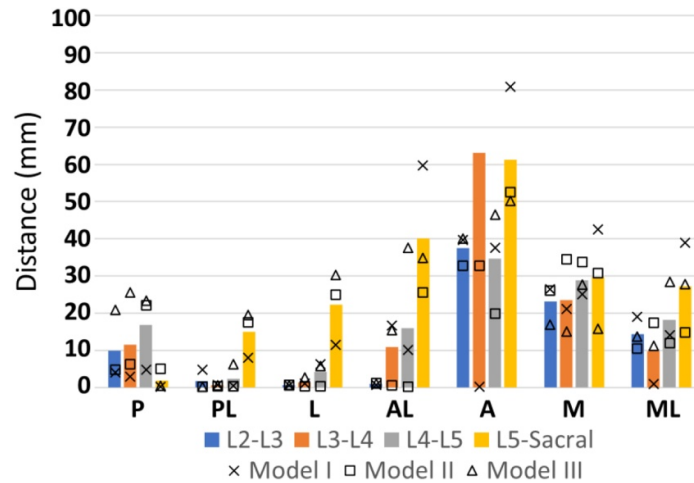


**Figure 8.** Compilation of distance measurements representing the spatial discrepancy between the global maximum intensity position, as calculated across the entire computational domain, and the target point as a function of target point region (horizontal axis), IVD level (vertical columns, color-coded), and anatomical model. The average distance value across models is given by the colored-bar, and the individual distances for each model is provided by the symbols, for each IVD level and target point region combination. Non-zero values of distance indicate that in addition to the focal intensity distribution and gain at the specified target point, an additional secondary intensity peak of higher magnitude was generated spatially apart from the target.

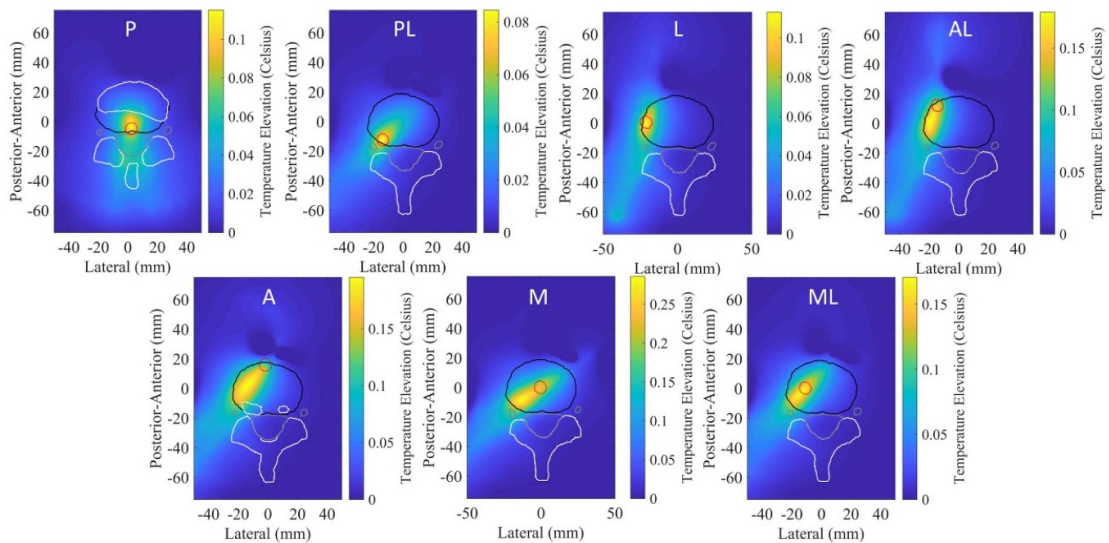
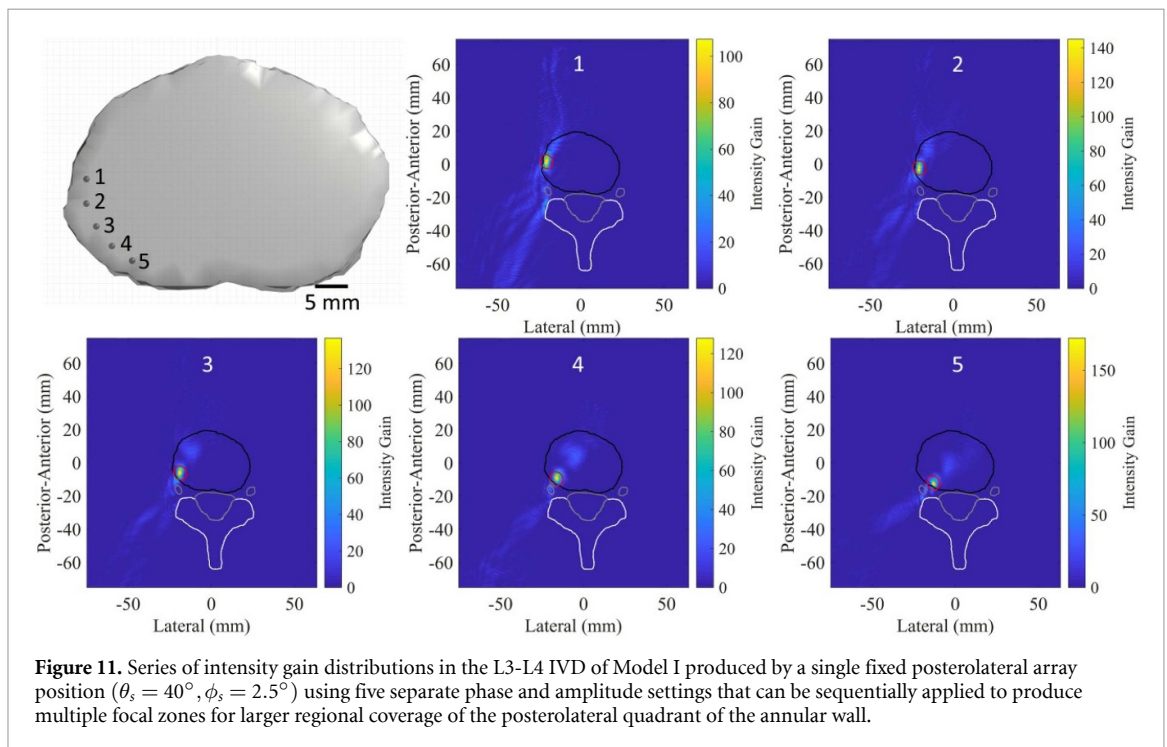
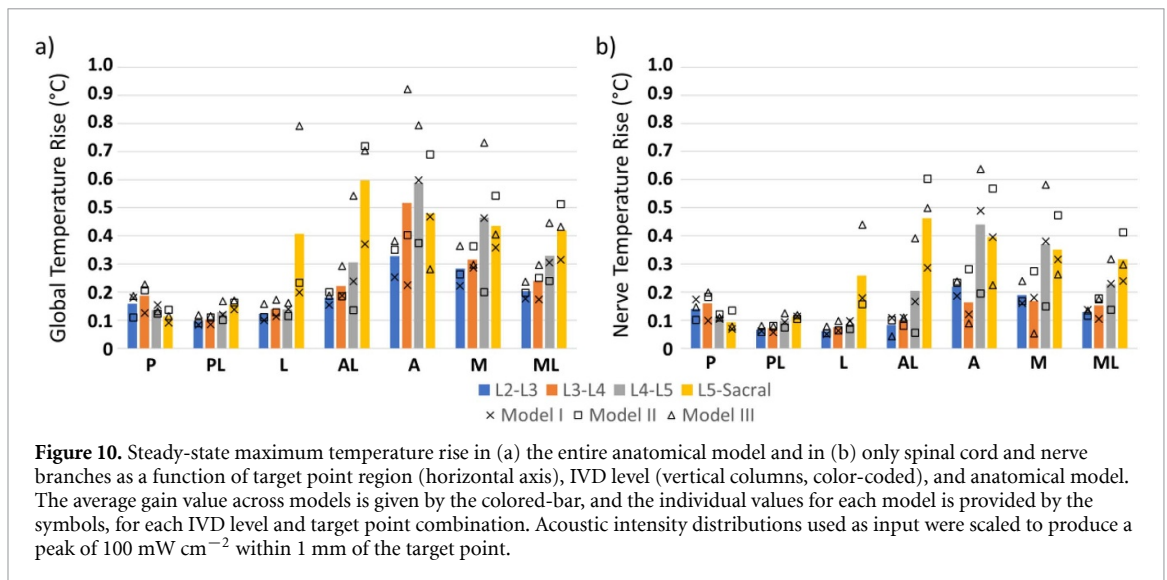


**Figure 9.** Steady-state temperature rise distributions resulting from the intensity profiles of figure 6 scaled to a peak  $I_{SPTA}$  of  $100 \text{ mW cm}^{-2}$  within 1 mm of the target point, shown for the L3-L4 IVD of Model I, for all seven target point regions as labeled. Anatomical boundaries are contoured for bone (white), IVD (black) and spinal cord and nerve branches (grey). The target point is spatially located at the center of the red contour.

broader, particularly for anterior, medial, and mediolateral targets. As such these sites may not represent ideal targets for highly localized and spatially accurate energy delivery, but could be suitable for more regional/volumetric exposure of the disc. In terms of the vertebral levels, L2-L3 and L3-L4 IVDs showed the highest intensity gain across all target point regions, with the exception of the posterior target, which was maximum for the L5-S1 IVD. This is likely due to the larger posterior window between spinous processes at the L5-S1 level. Greatest localization capabilities in L2-L3 and L3-L4 agrees with the findings of Qiao *et al* (2019), and is likely due to the minimized shadowing effects of hip and rib bone structures at these levels. The peak temperature elevations corresponding to a representative LIPUS target exposure of  $100 \text{ mW cm}^{-2}$   $I_{SPTA}$ , as shown in figure 10, were  $<1 \text{ }^\circ\text{C}$  and thereby below thermal toxicity thresholds for all investigated target point and anatomical model combinations. The reported temperature rise values can also be scaled linearly with target treatment intensity, and thus can be used to bracket LIPUS exposure intensity limits to maintain safe levels of thermal elevation.



Positioning an extracorporeal phased array to facilitate targeted energy delivery to the IVD is inherently complex due to sometimes limiting acoustic windows along with the strong attenuating and beam-distorting effects of nearby irregular spinal bone geometry. For each target point and model combination explored herein the phased array was iteratively rotated about the model body axes to identify the position resulting in the maximum energy summation across the array surface, derived from the backwards virtual source pressure emissions. Although other studies have shown feasibility of sonicating directly through the posterior arch and lamina bone regions of thoracic vertebrae using an extracorporeal transducer to focus within the spinal column (Xu and O'Reilly 2018, 2020), here the employed array placement scheme favored acoustic windows and transmission pathways directly to the IVD that were non-incident with bone. Further, using element amplitude weightings for the forward simulations derived from the backwards pressure distributions served to further minimize contributions of elements that had beam paths incident with bone structures. Alternative means of assigning amplitude weightings, such as uniform weighting or an amplitude compensation scheme that renormalizes the distorted transmitted contributions from all elements (White *et al* 2005) could lead to greater off-target energy deposition and heating in intervening bone. Optimal array placements determined herein had similar trends across Models: for IVDs in higher vertebral levels (L2-L5), posterior array placement with a transforaminal pathway was determined for posterior IVD target access,



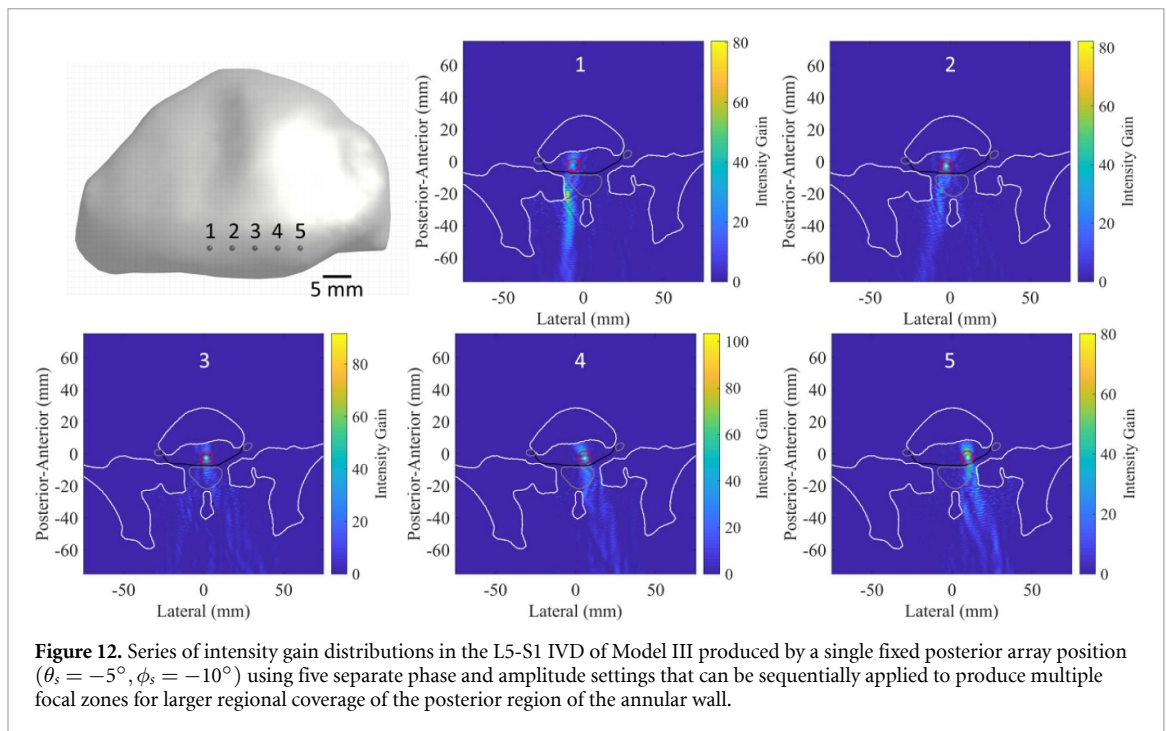


**Figure 12.** Series of intensity gain distributions in the L5-S1 IVD of Model III produced by a single fixed posterior array position ( $\theta_s = -5^\circ$ ,  $\phi_s = -10^\circ$ ) using five separate phase and amplitude settings that can be sequentially applied to produce multiple focal zones for larger regional coverage of the posterior region of the annular wall.

and posterolateral array placement determined for all other targets; for the L5-S1 IVD, where shadowing from the hip bone was more dominant, posterior array placement and transforaminal acoustic pathways were determined for most IVD target regions. While the transforaminal pathway lead to greater acoustic energy deposition in the spinal canal compared to posterolateral array placement, the anticipated peak intensities and temperature elevation in the canal for these cases ( $50\text{--}426\text{ mW cm}^{-2}$ ,  $0.07\text{--}0.6\text{ }^\circ\text{C}$  for  $100\text{ mW cm}^{-2}$   $I_{\text{SPTA}}$  target LIPUS) are low in relation to pressure/intensity magnitudes safely applied for reversible blood-spinal cord or blood-brain barrier opening (Downs *et al* 2015, Payne *et al* 2017, Fletcher *et al* 2019), and temperatures well below those necessary to induce irreversible thermal tissue damage to the spinal cord (Haveman *et al* 2005). Although unexplored herein, it is likely that acoustic windows and optimal array placements would be affected by alternative patient positions. In particular, transforaminal acoustic windows may be enlarged and improved through flexion of the spine to increase the gap between spinal processes (Xu and O'Reilly 2020).

Differences in simulation results between the three anatomical models used in this study demonstrate that anatomical variability has a significant influence in the achievable localization of extracorporeal ultrasound energy. In terms of intensity gain, the distance between the array and the target is one key factor expected from fundamental acoustics, and a general trend of greater intensity gain in IVD regions and Models with lower array-target depth was seen (figure 7). This distance is constrained by overall body size, though perhaps more specifically, by the curvature and position of the spine in the body relative to the posterior skin boundary, as seen in Model II, which had larger overall average intensity gain and lower average array-target distance compared to Model III (49.6 and 12.1 cm, vs. 31.1 and 13.1 cm) despite similar waist perimeter measurements (95 cm vs 96 cm). IVD height is likely also a critical factor, particularly in more central and anterior IVD target regions that require beam propagation between vertebrae and through the IVD to access. While disc heights were generally similar across all Models (table 1), the L4-L5 IVD of Model II was the shortest of all modeled IVDs and had the lowest overall average intensity gain across all target points compared to the other L4-L5 IVDs (60.9, 33.3, and 34.9 for Model I, II, and III, respectively). As a result, it may be more difficult to localize energy within central/anterior regions of IVDs in patients with heavily degenerated IVDs and associated reduced disc height. The overall structure/geometry of the spine and surrounding bones is also important, with more constrained acoustic windows caused by narrower gaps between bones/vertebra and spinal processes to IVD targets likely leading to worse energy localization capabilities. For instance, greater shadowing of the L4-L5 IVD by the hip and iliac crest in Model III compared to the other Models (table 1) may have contributed to its lower overall intensity gain and greater off-target peak intensity spatial disparities results. Hip shadowing also limited lateral access to the L5-S1 disc in all models, resulting in constrained transforaminal acoustic propagation which contributed to the poorer localization of energy to all except the most posterior target points compared to other IVDs. In future modeling analyses of this approach, inclusion of larger numbers of patient anatomies and spine geometries is



warranted to better bracket expected performance across a broader population. Anatomical models with varying degrees of disc degeneration/herniation should also be considered and could be informative in determining which particular stages of disease progression are most advantageous for facilitating extracorporeal ultrasound and LIPUS delivery. Given the variability in energy localization capabilities between the target points and three anatomical models studied herein, similar modeling approaches or other pre-treatment planning methods to assess targetability of a given site may be necessary for effective clinical application.

Simulations of multi-target focusing demonstrate the capability of sequentially applying different phase/amplitude illumination patterns to increase spatial coverage of ultrasound energy to the target IVD region, for a stationary array position. While the field patterns illustrated in figures 11 and 12 demonstrate overall peripheral zone coverage extending ~25 mm long, they are not exhaustive, and larger coverage zones consisting of additional focal spots or focal spots further apart may permit larger spatial coverage. Rapid temporal switching of ~4–5 single-focus illumination patterns, as demonstrated herein, would be suitable for interleaved pulsed exposure regimens typical of LIPUS treatments (~20%–25% duty cycle). Alternatively, methods for generating multi-focal illumination patterns for simultaneous exposure of larger regions could be applied (Ebbini and Cain 1989). Other means of increasing volumetric coverage could include lowering the frequency and/or apodizing or reducing the overall active footprint of the array to increase the wavelength and produce broader focal patterns, respectively, although such designs would likely result in poorer target gain and energy localization capabilities. Similar to the demonstrated broader intra-disc distributions produced in anterior/medial IVD targets (figure 6), contralateral placement of the array and directing energy along longer path lengths through the IVD to target regions could also enhance overall IVD spatial coverage.

Although this study demonstrates promising capabilities of a generic planar phased array for LIPUS delivery to IVDs, particularly to proximal-lateral regions of the annulus fibrosus, performance to central and anterior regions could likely be enhanced by adopting more specialized array designs. The array design employed in this study is similar to the Exablate 2100 Conformal Bone System array, which has a comparable geometry and footprint and consists of ~1000 channels operating at 550 kHz (Holbrook *et al* 2014, Cao *et al.* 2020). In practice, the phased array applicator configuration could be combined with robotic stereotactic manipulation platforms (Yiallouras and Damianou 2015), registered with imaging (CT/MRI) for planning/guidance, to practically achieve the array placements and orientations explored herein. Other studies investigating extracorporeal ultrasound delivery to the spine proposed bilateral curvilinear arrays surrounding the posterolateral aspects of the body, geometrically aligned within the center of the IVD or spinal canal (Qiao *et al* 2019, Xu and O'Reilly 2020). The bilateral design would increase energy localization within medial regions of the IVD, with simulations from Qiao *et al* demonstrating greater achievable pressure gains in the center nucleus compared to the unilateral approach and planar array investigated in this study (2019). However, capabilities of delivering energy to off-centered or multiple targets within the IVD using bilateral, geometrically curved array designs are uncertain. While geometrically curved array designs may provide more localized energy delivery, planar arrays have greater capabilities of electronically steering the beam away from the central axis, which could be beneficial for simultaneous exposure of multiple target points. In terms of general array specifications, a driving frequency of 500 kHz provides a good balance between penetration depth and wavelength size. Higher frequencies around 1–1.5 MHz that are typically used for LIPUS in orthopedic and soft tissue applications would likely be suboptimal in extracorporeal IVD treatment due to greater pre-focal attenuation and increasing absorption and tissue heating potential as frequency increases. Increasing the array dimensions and element density could increase energy localization and steering capabilities, and incorporating a second planar array for bilateral treatment would likely enhance energy localization within central and anterior IVD regions.

Future modeling studies of this approach could consider bilateral array schemes and include a more comprehensive investigation to optimize the array design and operating frequency for IVD energy delivery. Greater numbers of patient anatomies, patient positions, and target positions could be considered to obtain broader performance trends and inform treatment planning. While this study incorporated full-wave modeling of acoustic propagation through heterogeneous tissues, more complex analyses could incorporate mode conversion and shear wave propagation at soft tissue—bone interfaces. Further, additional tissue structures and compartments could be delineated (e.g. separation of the annulus fibrosus and nucleus in IVDs) for greater modeling accuracy, perhaps by using MRI image sets with enhanced soft-tissue contrast in combination with CT. Due to a lack of reliable measurements and characterization reported in literature for the acoustic properties in IVD tissue, here the properties of tendon/ligament were adopted, which are similar in composition to the concentric collagen lamellae of the outer annulus fibrosus. However, significantly greater acoustic attenuation within the nucleus of a degenerative disc could result in lower intensity gains than predicted in this study, particularly for more central and anterior target regions with longer beam path length within the IVD. Overall, this study supports the feasibility of extracorporeal delivery of LIPUS to

IVDs, particularly in posterior, posterolateral, and lateral regions of and adjacent to the annulus fibrosus. These sites are of high clinical importance, as they represent common injury locations for herniation and annular tears (Dulebohn *et al* 2019), as well as areas of post-discectomy surgical margins. While LIPUS has promising evidence from *in vitro* and *in vivo* animal studies to support its capability to enhance IVD repair and remodeling, additional preclinical and clinical evaluations of its utility for treating disc degeneration and herniation are warranted.

## 5. Conclusion

This study performed acoustic and biothermal simulations in 3D anatomical models that demonstrated the capability of delivering targeted LIPUS to regions of lumbar IVDs spanning L2-S1 vertebral levels using an extracorporeal planar phased array positioned posterior or posterolateral to the body. Time reversal methods were used to determine optimal placements of the array and driving phase/amplitude illumination patterns. Focal acoustic intensity gain was achieved in all target regions (range: 5–168), with enhanced localization of energy possible in posterior, posterolateral, and lateral peripheral regions of the discs (mean intensity gain >50) across anatomical models and IVD level. Greater intensity gain and energy localization capabilities were demonstrated in L2-L3 and L3-L4 IVDs compared to the lower L4-L5 and L5-S1 IVDs. Larger regional coverage of the IVD could be achieved by sequencing illumination patterns for different focal target positions at a fixed array position. Biothermal simulations demonstrated that LIPUS-appropriate exposures of  $100 \text{ mW cm}^{-2} I_{\text{SPTA}}$  to the target disc region would result in  $<1^\circ \text{C}$  global peak temperature elevation for all anatomical model and disc target region combinations. Hence, delivery of LIPUS to discrete regions of lumbar IVDs without significant off target energy deposition or heating is feasible and may be useful in clinical management of discogenic back pain.

## Acknowledgments

This work was supported by National Institutes of Health grant R21EB024347.

## ORCID iDs

Matthew S Adams  <https://orcid.org/0000-0001-8494-2684>

Chris J Diederich  <https://orcid.org/0000-0002-7260-6226>

## References

- Arts M P, Kuršumović A, Miller L E, Wolfs J F, Perrin J M, Van de Kelft E and Heidecke V 2019 Comparison of treatments for lumbar disc herniation: systematic review with network meta-analysis *Medicine* **98** 11–21
- Aubry J, Pernot M, Marquet F, Tanter M and Fink M 2008 Transcostal high-intensity-focused ultrasound: ex vivo adaptive focusing feasibility study *Phys. Med. Biol.* **53** 2937
- Aubry J, Tanter M, Pernot M, Thomas J and Fink M 2003 Experimental demonstration of noninvasive transskull adaptive focusing based on prior computed tomography scans *J. Acoust. Soc. Am.* **113** 84–93
- Cao R, Huang Z, Nabi G and Melzer A 2020 Patient-specific 3-dimensional model for high-intensity focused ultrasound treatment through the rib cage *J. Ultrasound Med.* **39** 883–899
- Chen M, Sun J, Liao S, Tai P, Li T and Chen M 2015 Low-intensity pulsed ultrasound stimulates matrix metabolism of human annulus fibrosus cells mediated by transforming growth factor  $\beta$  1 and extracellular signal-regulated kinase pathway *Connective Tissue Res.* **56** 219–27
- Downs M E, Buch A, Sierra C, Karakatsani M E, Chen S, Konofagou E E and Ferrera V P 2015 Long-term safety of repeated blood-brain barrier opening via focused ultrasound with microbubbles in non-human primates performing a cognitive task *PLoS One* **10** e0125911
- Duck F A 2013 *Physical Properties of Tissues: A Comprehensive Reference Book* (New York: Academic)
- Dulebohn S C, Massa R N and Mesfin F B 2019 Disc herniation *StatPearls [Internet]* (Florida: StatPearls Publishing)
- Ebbini E S and Cain C A 1989 Multiple-focus ultrasound phased-array pattern synthesis: optimal driving-signal distributions for hyperthermia *IEEE Trans. Ultrason. Ferroelectr. Freq. Control* **36** 540–8
- Eliasberg C D, Kelly M P, Ajiloye R M and Soohoo N F 2016 Complications and rates of subsequent lumbar surgery following lumbar total disc arthroplasty and lumbar fusion *Spine* **41** 173
- Fink M 1992 Time reversal of ultrasonic fields. I. Basic principles *IEEE Trans. Ultrason. Ferroelectr. Freq. Control* **39** 555–66
- Fink M, Montaldo G and Tanter M 2004 Time reversal acoustics *IEEE Ultrasonics Symp., 2004*
- Fletcher S P, Ogronnik N and O'Reilly M A 2020 Enhanced detection of bubble emissions through the intact spine for monitoring ultrasound-mediated blood-spinal cord barrier opening *IEEE Trans. Biomed. Eng.* **67** 1387–96
- Fujii K, Yamazaki M, Kang J D, Risbud M V, Cho S K, Qureshi S A, Hecht A C and Iatridis J C 2019 Discogenic back pain: literature review of definition, diagnosis, and treatment *J. Bone Miner. Res.* **3** e10180
- Goubert L, Crombez G and De Bourdeaudhuij I 2004 Low back pain, disability and back pain myths in a community sample: prevalence and interrelationships *Eur. J. Pain* **8** 385–94
- Haemmerich D, Wright A W, Mahvi D M, Jr FT L and Webster J G 2003 Hepatic bipolar radiofrequency ablation creates coagulation zones close to blood vessels: a finite element study *Med. Biol. Eng. Comput.* **41** 317–23

- Harrison A, Lin S, Pounder N and Mikuni-Takagaki Y 2016 Mode & mechanism of low intensity pulsed ultrasound (LIPUS) in fracture repair *Ultrasonics* **70** 45–52
- Hasgall P A, Di Gennaro F, Baumgartner C, Neufeld E, Lloyd B, Gosselin M C, Payne D, Klingenberg A and Kuster N 2018 IT'IS database for thermal and electromagnetic parameters of biological tissues Version 4.0.
- Haveman J, Sminia P, Wondergem J, van der Zee J and Hulshof M 2005 Effects of hyperthermia on the central nervous system: what was learnt from animal studies? *Int. J. Hyperth.* **21** 473–87
- Helm S, Simopoulos T, Stojanovic M, Abdi S and Terany M 2017 Effectiveness of thermal annular procedures in treating discogenic low back pain *Pain Phys.* **20** 447–70
- Hiyama A, Mochida J, Iwashina T, Omi H, Watanabe T, Serigano K, Iwabuchi S and Sakai D 2007 Synergistic effect of low-intensity pulsed ultrasound on growth factor stimulation of nucleus pulposus cells *J. Orthop. Res.* **25** 1574–81
- Holbrook A B, Ghanouni P, Santos J M, Dumoulin C, Medan Y and Pauly K B 2014 Respiration based steering for high intensity focused ultrasound liver ablation *Magn. Reson. Med.* **71** 797–806
- Hynynen K 1990 Biophysics and technology of ultrasound hyperthermia *Methods of External Hyperthermic Heating* eds M Gautherie (Berlin: Springer) pp 61–115
- Iwabuchi S, Ito M, Chikanishi T, Azuma Y and Haro H 2008 Role of the tumor necrosis factor- $\alpha$ , cyclooxygenase-2, prostaglandin E<sub>2</sub>, and effect of low-intensity pulsed ultrasound in an in vitro herniated disc resorption model *J. Orthop. Res.* **26** 1274–8
- Iwabuchi S, Ito M, Hata J, Chikanishi T, Azuma Y and Haro H 2005 In vitro evaluation of low-intensity pulsed ultrasound in herniated disc resorption *Biomaterials* **26** 7104–14
- Iwashina T, Mochida J, Miyazaki T, Watanabe T, Iwabuchi S, Ando K, Hotta T and Sakai D 2006 Low-intensity pulsed ultrasound stimulates cell proliferation and proteoglycan production in rabbit intervertebral disc cells cultured in alginate *Biomaterials* **27** 354–61
- Jiang X, Savchenko O, Li Y, Qi S, Yang T, Zhang W and Chen J 2019 A review of low-intensity pulsed ultrasound for therapeutic applications *IEEE Trans. Biomed. Eng.* <https://doi.org/10.1109/TBME.2018.2889669>
- Katz J N 2006 Lumbar disc disorders and low-back pain: socioeconomic factors and consequences *J. Bone Joint Surg.* **88** 21–24
- Kobayashi Y, Sakai D, Iwashina T, Iwabuchi S and Mochida J 2009 Low-intensity pulsed ultrasound stimulates cell proliferation, proteoglycan synthesis and expression of growth factor-related genes in human nucleus pulposus cell line *Eur. Cell Mater.* **17** 15–22
- Lotz J C, Haughton V, Boden S D, An H S, Kang J D, Masuda K, Freemont A, Berven S, Sengupta D K and Tanenbaum L 2012 New treatments and imaging strategies in degenerative disease of the intervertebral disks *Radiology* **264** 6–19
- Malik K M, Cohen S P, Walega D R and Benzoni H T 2013 Diagnostic criteria and treatment of discogenic pain: a systematic review of recent clinical literature *Spine J.* **13** 1675–89
- Marquet F, Pernot M, Aubry J F, Montaldo G, Marsac L, Tanter M and Fink M 2009 Non-invasive transcranial ultrasound therapy based on a 3D CT scan: protocol validation and in vitro results *Phys. Med. Biol.* **54** 2597
- Martin E, Jeanmonod D, Morel A, Zadicario E and Werner B 2009 High-intensity focused ultrasound for noninvasive functional neurosurgery *Ann. Neurol.* **66** 858–61
- Muir T G and Carstensen E L 1980 Prediction of nonlinear acoustic effects at biomedical frequencies and intensities *Ultrasound Med. Biol.* **6** 345–57
- Nicholson P, Haddaway M J and Davie M 1994 The dependence of ultrasonic properties on orientation in human vertebral bone *Phys. Med. Biol.* **39** 1013
- Omi H, Mochida J, Iwashina T, Katsuno R, Hiyama A, Watanabe T, Serigano K, Iwabuchi S and Sakai D 2008 Low-intensity pulsed ultrasound stimulation enhances TIMP-1 in nucleus pulposus cells and MCP-1 in macrophages in the rat *J. Orthop. Res.* **26** 865–71
- Payne A H, Hawryluk G W, Anzai Y, Odén H, Ostlie M A, Reichert E C, Stump A J, Minoshima S and Cross D J 2017 Magnetic resonance imaging-guided focused ultrasound to increase localized blood-spinal cord barrier permeability *Neural Regen. Res.* **12** 2045
- Peng B 2013 Pathophysiology, diagnosis, and treatment of discogenic low back pain *World J. Orthop.* **4** 42
- Pounder N M and Harrison A J 2008 Low intensity pulsed ultrasound for fracture healing: a review of the clinical evidence and the associated biological mechanism of action *Ultrasonics* **48** 330–8
- Qiao S, Elbes D, Boubriak O, Urban J, Coussios C C and Cleveland R O 2019 Delivering focused ultrasound to intervertebral discs using time-reversal *Ultrasound Med. Biol.* **45** 2405–16
- Risbud M V and Shapiro I M 2014 Role of cytokines in intervertebral disc degeneration: pain and disc content *Nat. Rev. Rheumatol.* **10** 44
- Scott S J, Salgaonkar V, Prakash P, Burdette E C and Diederich C J 2014 Interstitial ultrasound ablation of vertebral and paraspinal tumours: parametric and patient-specific simulations *Int. J. Hyperth.* **30** 228–44
- Shaheed C A, Maher C G, Williams K A and Mclachlan A J 2014 Interventions available over the counter and advice for acute low back pain: systematic review and meta-analysis *J. Pain* **15** 2–15
- Shu B, Yang Z, Li X and Zhang L 2012 Effect of different intensity pulsed ultrasound on the restoration of rat skeletal muscle contusion *Cell Biochem. Biophys.* **62** 329–36
- Sparrow K J, Finucane S D, Owen J R and Wayne J S 2005 The effects of low-intensity ultrasound on medial collateral ligament healing in the rabbit model *Am. J. Sports Med.* **33** 1048–56
- Takakura Y, Matsui N, Yoshiya S, Fujioka H, Muratsu H, Tsunoda M and Kurosaka M 2002 Low-intensity pulsed ultrasound enhances early healing of medial collateral ligament injuries in rats *J. Ultrasound Med.* **21** 283–8
- Thomas J and Fink M A 1996 Ultrasonic beam focusing through tissue inhomogeneities with a time reversal mirror: application to transskull therapy *IEEE Trans. Ultrason. Ferroelectr. Freq. Control* **43** 1122–9
- White J, Clement G T and Hynynen K 2005 Transcranial ultrasound focus reconstruction with phase and amplitude correction *IEEE Trans. Ultrason. Ferroelectr. Freq. Control* **52** 1518–22
- Xu R and O'Reilly M A 2018 Simulating transvertebral ultrasound propagation with a multi-layered ray acoustics model *Phys. Med. Biol.* **63** 145017
- Xu R and O'Reilly M A 2020 A spine-specific phased array for transvertebral ultrasound therapy: design and simulation *IEEE Trans. Biomed. Eng.*
- Yiallouras C and Damianou C 2015 Review of MRI positioning devices for guiding focused ultrasound systems *Int. J. Med. Robot Comp.* **11** 247–55
- Zhang Y, Guo T, Guo X and Wu S 2009 Clinical diagnosis for discogenic low back pain *Int. J. Biol. Sci.* **13** 647–58